Improved Finite-State Model Predictive Current Control With Zero-Sequence Current Suppression for OEW-SPMSM Drives

Xin Yuan, Shuo Zhang, *Member, IEEE*, Chengning Zhang, Michele Degano, *Member, IEEE*, Giampaolo Buticchi, *Senior Member, IEEE*, and Alessandro Galassini, *Member, IEEE*

***Abstract*—In order to suppress zero-sequence current (ZSC) for open-end winding surfaced permanent magnet synchronous machine (OEW-SPMSM) drives with single dc voltage source, many methods have been employed. Actual solutions imply either proportional-integral-based control or direct torque control cannot present the characteristic of fast dynamic responses and low torque ripples at the same time. Hence, finite-state model predictive current control (FS-MPCC) based on a cost function with ZSC suppression was proposed. To suppress model parameter mismatch, many previous works have proposed related strategies but few work considered zero-sequence parameter disturbances such as zero-sequence inductance, resistance, and rotor flux linkage disturbances. This article improves the ZSC prediction model based on the previous ZSC errors and zero-sequence voltage deviations, and at the same time ZSC is reduced. A comparison between the conventional FS-MPCC and the improved one is carried out in simulation and experiment to verify the effectiveness of the proposed FS-MPCC scheme.**

***Index Terms*—Finite-state model predictive current control (FS-MPCC), open-end winding surfaced permanent magnet synchronous machine (OEW-SPMSM), parameter mismatch, zero-sequence current (ZSC) suppression.**

NOMENCLATURE

ω_e, ω_m	Electrical and mechanical angular speed.
T_e, T_l	Electromagnetic torque and load torque.
J, B	Inertia and viscous friction coefficient.
p	Number of pole pairs.
R_s	Motor stator resistance.
L_s	Motor stator inductance.
Ψ_m	Motor rotor flux linkage.
$\overline{R_s}$	Initial nominal zero-sequence resistance.
$\overline{L_0}$	Initial nominal zero-sequence inductance.
$\overline{\Psi_{3m}}$	Initial nominal zero-sequence flux linkage.
T_s	System sampling time.
θ_r	Electrical rotor angle.
Ψ_s	Motor stator flux linkage vectors.
L_0	Motor zero-sequence inductance.
Ψ_{3m}	Motor zero-sequence flux linkage.

Manuscript received April 9, 2019; revised July 18, 2019; accepted September 11, 2019. Date of publication September 17, 2019; date of current version February 11, 2020. This work was supported in part by the National Natural Science Foundation of China under Grant 51677005 and in part by Research and development plan in key areas of Guangdong province under Grant 2019B090910001. Recommended for publication by Associate Editor H. Hofmann. *(Corresponding author: Shuo Zhang.)*

X. Yuan, S. Zhang, and C. Zhang are with the School of Mechanical Engineering and Collaborative Innovation Center of Electric Vehicles in Beijing, Beijing Institute of Technology, Beijing 100081, China (e-mail: yuanxinedu@gmail.com; shuozhangxd@163.com; chengningzhangIEEE@163.com).

M. Degano and A. Galassini are with the Power Electronics, Machines and Control Group, University of Nottingham, Nottingham NG7 2RD, U.K. (e-mail: michele.degano@nottingham.ac.uk; alessandro.galassini@nottingham.ac.uk).

G. Buticchi is with the Power Electronics, Machines and Control Group, University of Nottingham Ningbo China, Ningbo 315100, China (e-mail: giampaolo.buticchi@nottingham.edu.cn).

Color versions of one or more of the figures in this article are available online at http://ieeexplore.ieee.org.

Digital Object Identifier 10.1109/TPEL.2019.2942156

I. INTRODUCTION

THE open-end winding machine (OEWM) faced a growing interest owing to its high power output, good fault-tolerance, and wide speed range capability [1]. The OEWM is realized by opening the neutral point of the stator winding and connecting each side of it to a power converter. This kind of OEWMs are mainly divided into three parts, namely, OEW-reluctance [1], OEW-induction [2], and OEW-permanent magnet synchronous machines (OEW-PMSMs). Since OEW-surfaced permanent magnet synchronous machines (OEW-SPMSMs) possess the merits of simple control mode and high torque density, they are regarded as a control object in this article [3]. Several control strategies for the OEWM have been proposed and will be reviewed in Section II. Section III describes the OEW-SPMSM drive system specifications. Considering that the main challenges for the application are the suppression of the zero-sequence current (ZSC) and fast dynamic response, Section IV presents a conventional finite-state model predictive current control (FS-MPCC) [25] and [26]. However, the existing FS-MPCC literatures only focused on the reduction of weight factors and calculation. In Section V-A, it can be seen that zero-sequence model parameter can affect the current control performance. Therefore, this article addresses this problem in the red color area of Fig. 1. The contribution is that without employing observers to evaluate a zero-sequence model [30]–[32] or utilizing compensators to eliminate the disturbances cause by zero-sequence model [15]–[17], a novel zero-sequence model based on the previous ZSC and zero-sequence voltage (ZSV), stored in a memory space is proposed. The detailed procedure of the proposed algorithm is described in Section V-B. To validate the effectiveness of the proposed method, the performance of conventional FS-MPCC scheme and proposed

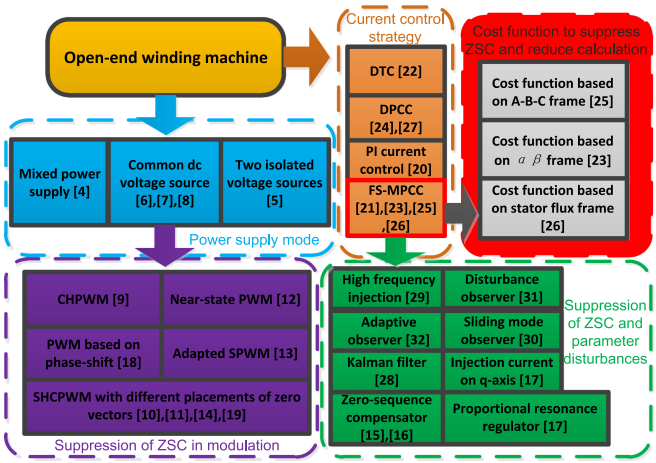

Fig. 1. Diagram of literature review.

FS-MPCC scheme is observed in Sections VI and VII. Finally, the conclusions are derived in Section VIII.

II. Literature Review

Fig. 1 shows a summary of some specific methods presented in the literature. From the perspective of power supply mode, the OEWM topology is mainly divided into a common dc bus, two isolated dc voltage sources, and mixed power supply topology. The mixed power supply topology consists of a capacitor and dc voltage source [4]. The OEWM with two isolated dc voltage sources needs to employ two sets of dc voltage sources, but can avoid the generation of zero-sequence path [5]. However, this topology leads to high size and cost. OEWMs with common dc bus only need one set of dc voltage source, but zero-sequence path in the system cannot be avoided. In the OEWMs with common dc bus, it can be categorized into several types, namely, a combination of a semicontrolled inverter and full controlled inverter [6] and [7], combination of two full controlled inverters. Due to more voltage vectors available, OEWMs drives with the combination of two full controlled two-level converters have received more attention. Zhang and Wang [8] noted the presence of both ZSV and third harmonic sinusoidal back-electromotive force (EMF) in the zero-sequence path. ZSC is forced to be generated by the ZSV sources. It cannot improve the control performance, but increase the losses of the machine and inverter.

To suppress ZSC, many researchers have proposed effective methods. The pioneering work of Dr. M. R. Baiju adopted a central hexagon modulation pulsewidth modulation (PWM) (CHPWM) strategy to eliminate ZSC [9]. It has been noted that there are six vertexes of a hexagon that cannot generate ZSV in the zero-sequence path. In this case, hexagon voltage vectors are only employed to compose the desired voltage vector, which can reduce the amplitude of ZSC. However, some extra voltage vectors cannot be utilized and the maximum voltage dc bus utilization cannot be achieved. Somasekhar and Srinivas [10] noted that the placement of two zero vectors can cause different value of ZSV. Within one switching period, the appropriate distribution time of zero vectors can force the average value of ZSV to zero based on the principle of volt-second balance. On this basis, subhexagonal center PWM scheme was proposed to suppress ZSV. Somasekhar and Srinivas [11] added the appropriate distribution time of zero vectors into decoupled space-vector PWM scheme to annihilate ZSV. Un and Hava [12] proposed a novel near-state modulation strategy to reduce the ZSC. Enhancing system efficiency, Kiadehi *et al.* [13] presented an adapted SPWM modulation strategy to suppress ZSC. Zhou and Nian [14] noted that the machine rotor flux linkage contains rich harmonic ripples, which can leads to high order terms of zero-sequence back EMF. Wang *et al.* [15] established an active compensator to suppress zero-sequence back EMF. The active compensator consists of two main parts, namely, a third harmonic phase-locked loop and new current regulator. However, this method was only applied in a half-controlled converter based on an OEW-permanent magnet synchronous generator. Hwang and Wei [16] employed a ZSC estimator to predict ZSC and suppress zero-sequence back EMF. Nian and Hu [17] adopted a q-axis current injection method and proportional resonance regulator to suppress zero-sequence EMF and ZSC. Oleschuk *et al.* [18] presented a PWM with phase-shift-based to suppress ZSV. However, in [19], it has been noted that the phase-shift-based synchronous modulation would lead to extra ZSV due to in the dead time inverters.

Compared with classical proportional-integral (PI)-based control [20], predictive control has gained widely visibility in recent years owing to the characteristic of the fast dynamic response. Moreover, predictive control scheme can avoid the process of tuning PI coefficient [21]. Direct torque control has a good dynamic response but the torque ripples are high [22]. In pioneering works with predictive current control, the main classification given is: FS-MPCC and deadbeat predictive current control (DPCC) [23] and [24]. The principle of FS-MPCC is to predict future motor behavior and then select an optimum voltage vector based on cost function minimization. Zhu *et al.* [25] proposed a novel FS-MPCC based on A–B–C frame to suppress ZSC and avoid weight factors. Moreover, the computation burden is reduced significantly. Chong *et al.* [26] presented a novel FS-MPCC based on a flux vector prediction observer, but the topology is two isolated dc voltage sources. In a conventional DPCC, the predicted voltage is applied in inverters through space vector pulse modulation without any cost functions, and the switching frequency is fixed [27]. The performances of FS-MPCC and DPCC mainly depend on model parameters. Once model parameters are inaccurate, the performance of torque ripples and currents is deteriorated dramatically [28] and [29]. Some researchers have presented many methods to suppress the disturbances caused by parameter mismatch [30] and [31]. However, there are few works to suppress zero-sequence model parameter disturbances. Yuan *et al.* [32] presented a novel adaptive sliding mode observer to suppress the zero-sequence model parameter disturbances, but this method is only applied in DPCC scheme.

III. OEW-SPMSM Drive With Common DC Bus

A. Topology of OEW-SPMSM Drive With Common DC Bus

The OEW-SPMSM is constructed by opening the star point, leaving the six terminals of the stator winding available. In this

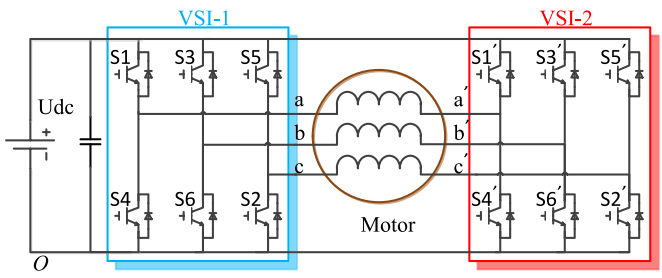

Fig. 2. Single dc-link dual-VSI fed OEW-SPMSM.

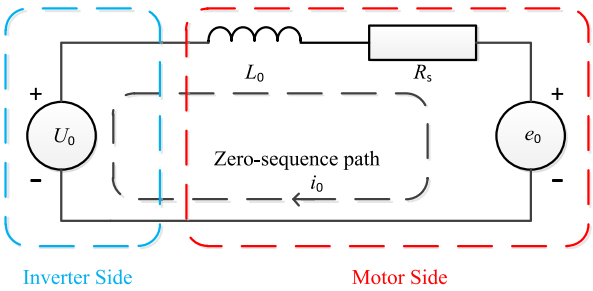

Fig. 3. Equivalent zero sequence circuit.

article, dual two-level voltage-source inverter (VSI) topology is adopted and total possible switching combinations in the dual inverter can reach to 64 ($2^3 \times 2^3$). The OEW-SPMSM drive with common dc bus is illustrated in Fig. 2. Because OEW-SPMSM drive is supplied by single dc voltage, there is a zero-sequence path in the system, which is presented in Fig. 3.

B. Mathematical Model of OEW-SPMSM

In this article, to simplify the mathematical model, some factors such as the cogging torque, magnetic saturation, and magnetic hysteresis losses are neglected. In addition, because a zero-sequence path exists in the system, the mathematical model of OEW-SPMSM equations in $\alpha\beta 0$ stationary frame is different from that of traditional SPMSMs, which can be presented as [24]

$$U_s = R_s i_s + \frac{d\psi_s}{dt} \tag{1}$$

$$\psi_s = L_s i_s + \psi_m e^{j\theta_r} \tag{2}$$

$$U_0 = R_s i_0 + L_0 \frac{di_0}{dt} + e_0 \tag{3}$$

$$i_0 = \frac{i_A + i_B + i_C}{3} \tag{4}$$

$$e_0 = 3\omega_e \psi_{3m} \sin(3\theta_r) \tag{5}$$

$$T_e = 1.5p\left(\psi_m i_s - 6\psi_{3m}\sin(3\theta_r) i_0\right). \tag{6}$$

i_s and U_s stand for stator currents and voltage vectors, respectively; i_A, i_B, and i_C denote the a, b, and c phase stator currents. In the zero sequence path, U_0 and i_0 denote ZSV and ZSC, respectively; e_0 denotes zero-sequence back EMF. The mechanical equation of OEW-SPMSM is presented as

$$T_e - T_l = J\frac{d\omega_m}{dt} + B\omega_m. \tag{7}$$

IV. FS-MPCC Scheme With ZSC Suppression for OEW-SPMSM Drive

A. Current Prediction With Delay Compensation

According to (1) and (2), the voltage equation in stationary $\alpha\beta$ frame is presented as

$$U_s = L_s\frac{di_s}{dt} + R_s i_s + j\psi_m\omega_m p e^{j\theta_r}. \tag{8}$$

In digital controlled converters, discrete control is used. For the control realization, the system must be discretized. According to the first-order Euler discretization, the stationary prediction equation on $\alpha\beta$ frame is presented as

$$i_s(k+1) = i_s(k) + \frac{T_s}{L_s}\Big(U_s(k) - R_s i_s(k) - j\psi_m\omega_m(k)pe^{j\theta_r(k)}\Big). \tag{9}$$

Since ZSC exists in the system, according to (3)–(5), ZSC prediction equation can be presented as

$$i_0(k+1) = i_0(k) + \frac{T_s}{L_0}\left(U_0(k) - R_s i_0(k) - 3\omega_e(k)\psi_{3m}\sin(3\theta_r(k))\right). \tag{10}$$

Generally, there is a one-step control delay in the practical control system. Delay compensation needs to be considered in ZSC and stator currents, and these currents prediction equation are presented as

$$i_s(k+1) = \frac{T_s}{L_s}\Big(U_s(k) - R_s i_s(k) - j\psi_m\omega_m(k)pe^{j\theta_r(k)}\Big) + i_s(k) \tag{11}$$

$$i_s(k+2) = \frac{T_s}{L_s}\Big(U_s^{\mathrm{sw}=i}(k+1) - R_s i_s(k+1) - j\psi_m\omega_m(k+1)pe^{j\theta_r(k+1)}\Big) + i_s(k+1) \tag{12}$$

$$i_0(k+1) = \frac{T_s}{L_0}\left(U_0(k) - R_s i_0(k) - 3\omega_e(k)\psi_{3m}\sin(3\theta_r(k))\right) + i_0(k) \tag{13}$$

$$i_0(k+2) = \frac{T_s}{L_0}\left(U_0^{\mathrm{sw}=i}(k+1) - 3\omega_e(k+1)\psi_{3m}\sin(3\theta_r(k+1))\right) + i_0(k+1) - R_s\frac{T_s}{L_0} i_0(k+1) \tag{14}$$

where sw $= i$ means that the conducting mode in inverters is i. It should be noted that $i \in \{0, 1, \ldots, 25, 26\}$. $U_s^{\mathrm{sw}=i}(k+1)$ and $U_0^{\mathrm{sw}=i}(k+1)$ denote a selected stator voltage vector and ZSV with i conducting mode, respectively.

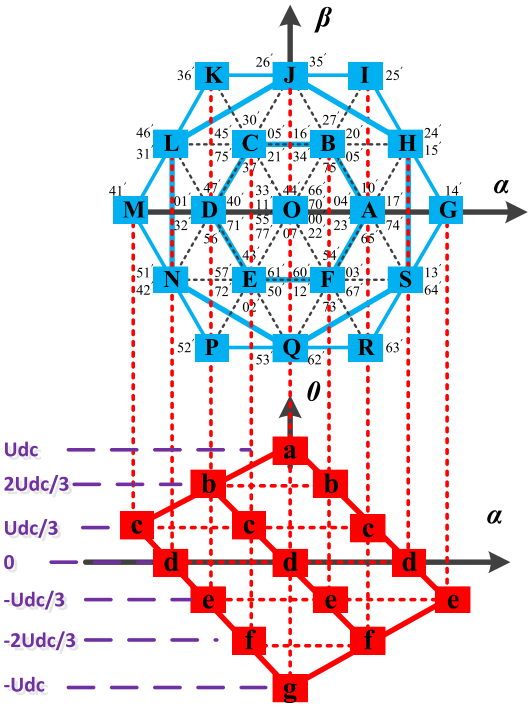

Fig. 4. Voltage vectors of dual-VSI in the view of $\alpha\beta$ and $\alpha 0$ plane.

B. Conducting Mode of OEW-SPMSM

In Fig. 4, it can be found that 18 nonzero vectors are located on the vertexes of three hexagons, including ABCDEF, HJLNQS, GIKMPR, and a zero vector O. There are seven different values of ZSV in $\alpha 0$ plane (abcdefg), namely $\pm U_{\rm dc}/3$, $\pm 2U_{\rm dc}/3$, $\pm U_{\rm dc}$, and 0. For example, the zero vector 0 can generate three types of ZSC with different switching combinations. The pioneering literatures have noted that the seven switching combinations OHJLNQS will not generate ZSV [9]. Table I shows 27 switching states and voltage vectors in stationary $\alpha\beta 0$ frame, where $S_a = 1$ means a phase leg of one inverter is conductive whereas $S_a = 0$ means a phase leg of one inverter is closed. It can be seen that some vectors in stationary $\alpha\beta$ frame can be linked with two different amplitude of ZSV in Table I.

C. Cost Function Minimization With ZSC Suppression

ZSC needs to be considered in the cost function and the FS-MPCC cost function $g(i)$ is given as

$$g(i) = \left|i_s^{\rm ref}(k+2) - i_s(k+2)\right| + w_0\left|i_0^{\rm ref}(k+2) - i_0(k+2)\right| \quad (15)$$

where $i_s^{\rm ref}(k+2)$, $i_0^{\rm ref}(k+2)$, $i_s(k+2)$, and $i_0(k+2)$ are the stator reference $\alpha\beta$ frame currents, reference ZSC, predicted $\alpha\beta$ frame currents, and predicted ZSC at the $(k+2)$th instant, respectively; w_0 is a weight factor of the cost function. Increasing w_0, the ZSC suppression turns to be major in the control object. To select the minimum value of the cost function, an optimal switching state can be obtained. In this case, $U_s^{{\rm sw}=i}(k+1)$ and $U_0^{{\rm sw}=i}(k+1)$ can be obtained according to Table I.

TABLE I
CONDUCTING MODE OF OEW-SPMSM

Conducting mode	Switching state (S_a, S_b, S_c, S_a', S_b', S_c')	U_0	U_α	U_β
0	(0,0,0,0,0,0)	0	0	0
1	(1,1,1,0,0,0)	$U_{\rm dc}$	0	0
2	(0,0,0,1,1,1)	$-U_{\rm dc}$	0	0
3	(1,0,0,0,0,0)	$U_{\rm dc}/3$	$2U_{\rm dc}/3$	0
4	(1,0,0,1,1,1)	$-2U_{\rm dc}/3$	$2U_{\rm dc}/3$	0
5	(1,1,0,0,0,0)	$2U_{\rm dc}/3$	$U_{\rm dc}/3$	$\sqrt{3}U_{\rm dc}/3$
6	(1,1,0,1,1,1)	$-U_{\rm dc}/3$	$U_{\rm dc}/3$	$\sqrt{3}U_{\rm dc}/3$
7	(0,1,0,0,0,0)	$U_{\rm dc}/3$	$-U_{\rm dc}/3$	$\sqrt{3}U_{\rm dc}/3$
8	(0,1,0,1,1,1)	$-2U_{\rm dc}/3$	$-U_{\rm dc}/3$	$\sqrt{3}U_{\rm dc}/3$
9	(0,1,1,0,0,0)	$2U_{\rm dc}/3$	$-2U_{\rm dc}/3$	0
10	(0,1,1,1,1,1)	$-U_{\rm dc}/3$	$-2U_{\rm dc}/3$	0
11	(0,0,1,0,0,0)	$U_{\rm dc}/3$	$-U_{\rm dc}/3$	$-\sqrt{3}U_{\rm dc}/3$
12	(0,0,1,1,1,1)	$-2U_{\rm dc}/3$	$-U_{\rm dc}/3$	$-\sqrt{3}U_{\rm dc}/3$
13	(1,0,1,0,0,0)	$2U_{\rm dc}/3$	$U_{\rm dc}/3$	$-\sqrt{3}U_{\rm dc}/3$
14	(1,0,1,1,1,1)	$-U_{\rm dc}/3$	$U_{\rm dc}/3$	$-\sqrt{3}U_{\rm dc}/3$
15	(1,0,0,0,1,1)	$-U_{\rm dc}/3$	$4U_{\rm dc}/3$	0
16	(1,1,0,0,0,1)	$U_{\rm dc}/3$	$2U_{\rm dc}/3$	$2\sqrt{3}U_{\rm dc}/3$
17	(0,1,0,1,0,1)	$-U_{\rm dc}/3$	$-2U_{\rm dc}/3$	$2\sqrt{3}U_{\rm dc}/3$
18	(0,1,1,1,0,0)	$U_{\rm dc}/3$	$-4U_{\rm dc}/3$	0
19	(0,0,1,1,1,0)	$-U_{\rm dc}/3$	$-2U_{\rm dc}/3$	$-2\sqrt{3}U_{\rm dc}/3$
20	(1,0,1,0,1,0)	$U_{\rm dc}/3$	$2U_{\rm dc}/3$	$-2\sqrt{3}U_{\rm dc}/3$
21	(1,0,0,0,0,1)	0	$U_{\rm dc}$	$\sqrt{3}U_{\rm dc}/3$
22	(1,1,0,1,0,1)	0	0	$2\sqrt{3}U_{\rm dc}/3$
23	(0,1,0,1,0,0)	0	$-U_{\rm dc}$	$\sqrt{3}U_{\rm dc}/3$
24	(0,0,1,1,0,0)	0	$-U_{\rm dc}$	$-\sqrt{3}U_{\rm dc}/3$
25	(0,0,1,0,1,0)	0	0	$-2\sqrt{3}U_{\rm dc}/3$
26	(1,0,1,0,0,1)	0	1	$\sqrt{3}U_{\rm dc}/3$

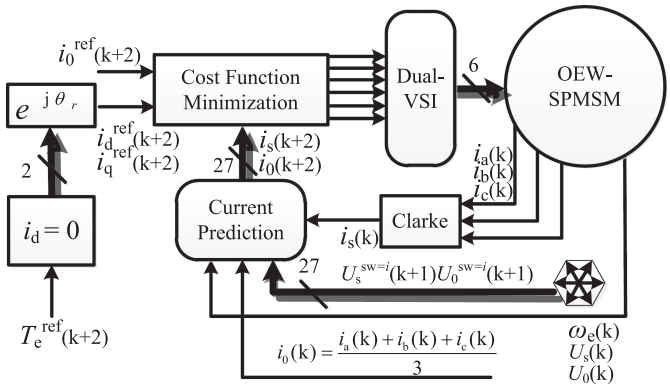

Fig. 5. Conventional FS-MPCC scheme with zero-sequence suppression for OEW-SPMSM drives.

Since the OEW-SPMSM is surface mounted, the inductance on dq-axis is the same, namely, $L_d = L_q = L_s$. Therefore, $i_d = 0$ control is adopted in FS-MPCC scheme and diagram of conventional FS-MPCC scheme in stationary $\alpha\beta 0$ frame is presented in Fig. 5.

V. Proposed FS-MPCC Scheme With Zero-Sequence Parameter Disturbances Suppression

A. Parameter Sensitivity Analysis for the Zero-Sequence Model

In the conventional FS-MPCC scheme, parameter disturbances can deteriorate the FS-MPCC scheme performance. Many previous methods have been employed to alleviate the disturbances caused by the parameter mismatch. However, in OEW-SPMSM drives, zero-sequence model parameters are also vital, and any inaccurate parameters can increase the value of ZSC. In addition, according to experimental results in Section VI, inaccurate zero-sequence parameter also can lead to large torque ripples and deteriorate *dq*-axis currents.

According to (10), it can be seen that R_s, Ψ_{3m}, and L_0 are zero-sequence parameters. As the stator temperature increases, the value of R_s rises. Vazquez *et al.* [27] and Feng *et al.* [28] have mentioned that high temperature in magnet can affect the variation of Ψ_{3m}. In addition, the value of L_0 can be affected with the stator current increasing. Therefore, in a practical situation, (10) needs to be turned into

$$i_0^p(k+1) = i_0(k) + \frac{T_s}{\overline{L_0}}\left(U_0(k) - \overline{R_s} i_0(k) - 3\omega_e(k)\overline{\psi_{3m}}\sin(3\theta_r(k))\right). \quad (16)$$

$i_0^p(k+1)$ is the predicted ZSC based on inaccurate zero-sequence model at the $(k+1)$th instant. In (16), it can be seen that there are deviations between the actual zero-sequence parameters and model parameters. This would lead to a nonoptimal switching state, which can deteriorate the FS-MPCC performance.

B. Novel Zero-Sequence Model

To deal with the aforementioned problem, a novel FS-MPCC scheme with zero-sequence parameter disturbances suppression is realized. The specific procedure of the proposed FS-MPCC scheme is presented as follows.

First, a current error between a measured current and predicted current based on the zero-sequence model at the *k*th instant need to be obtained. Subtracting (14) from (16) at the *k*th instant, the current error E_0 (k) can be presented:

$$\begin{aligned} E_0(k) &= i_0^p(k) - i_0(k) \\ &= \left(\frac{T_s}{\overline{L_0}} - \frac{T_s}{L_0}\right)U_0(k-1) - \left(\frac{T_s\overline{R_s}}{\overline{L_0}} - \frac{T_s R_s}{L_0}\right)i_0(k-1) \\ &\quad + \left(\frac{T_s\psi_{3m}}{L_0} - \frac{T_s\overline{\psi_{3m}}}{\overline{L_0}}\right)3\omega_e(k-1)\sin(3\theta_r(k-1)). \end{aligned} \quad (17)$$

Subtracting E_0 $(k-1)$ from E_0 (k), the error between E_0 (k) and E_0 $(k-1)$ can be presented in the following equation:

$$E_0(k) - E_0(k-1) \cong \left(\frac{T_s}{\overline{L_0}} - \frac{T_s}{L_0}\right)(U_0(k-1) - U_0(k-2)). \quad (18)$$

It should be noted that compared with ZSV terms variation at the adjacent sampling instant in (18), ZSC terms variation and electrical angular frequency terms variation plays a marginal role, which is explained as follows. First, electrical angular frequency cannot change significantly between adjacent sampling instants under the assumption of large motor inertial in low-speed machines. Thus, electrical angular frequency terms variation at the adjacent sampling instant can be approximately equal to zero. Second, in Table I, it can be seen that the minimum variation of ZSV between adjacent sampling instants is $\pm U_{\rm dc}/3$ except for 0 (the same ZSVs between adjacent sampling instants). Because the value of ZSC variation is quite smaller than the minimum variation of ZSV, ZSV terms variation in (18) is much larger than the ZSC terms variation. Hence, the variation of ZSC can be neglected in contrast with the variation of ZSV between adjacent sampling instants. The explanation for (18) is also presented in the simulation results in Section VI.

Considering the aforementioned note, a new parameter is defined as l in the proposed method. To get the l parameter, (19) can be presented:

$$l = \frac{T_s}{\overline{L_0}} - \frac{T_s}{L_0} = \frac{E_0(k) - E_0(k-1)}{(U_0(k-1) - U_0(k-2))} \quad (19)$$

where *l* is linked with the inductance variation between the real and initial nominal inductance. However, the value of dc-link voltage is not fixed in the operation, and it can lead to the fault for the estimated *l*. The reason is that, in (19), parameter *l* cannot be obtained when the denominator of (19) is zero. However, in the practical system, the denominator of (19) is not equal to zero when there are the same variation of ZSV at the adjacent instants. In this case, the estimation of the parameter l will be wrong. To avoid this, a new mechanism is introduced to solve the problem. Thanks to the minimum variation of ZSVs is $U_{\rm dc}/3$ from Table I, the variation of ZSVs at the adjacent instant is approximately equal or larger than $U_{\rm dc}/3$, when in theory the variation of ZSVs is not equal to zero. The acquisition of the parameter *l* is presented in Fig. 6.

Second, a zero-sequence model involved in stator resistance and third harmonic rotor flux linkage will be built based on the ZSC error at the adjacent instant. The detail procedures are introduced as follows. After obtaining the parameter *l*, the new predicted ZSC equation at the $(k+1)$th instant can be obtained as

$$i_0(k+1) = i_0^p(k+1) - E_0(k+1). \quad (20)$$

According to (18), the current error E_0 $(k+1)$ can be obtained as

$$E_0(k+1) \cong \left(\frac{T_s}{\overline{L_0}} - \frac{T_s}{L_0}\right)(U_0(k) - U_0(k-1)) + E_0(k). \quad (21)$$

It should be noted that E_0 $(k+1)$ contains the information of stator resistance and third harmonic rotor flux linkage, which can suppress the disturbances caused by the resistance and third harmonic rotor flux linkage mismatch. Substituting (21) in (20),

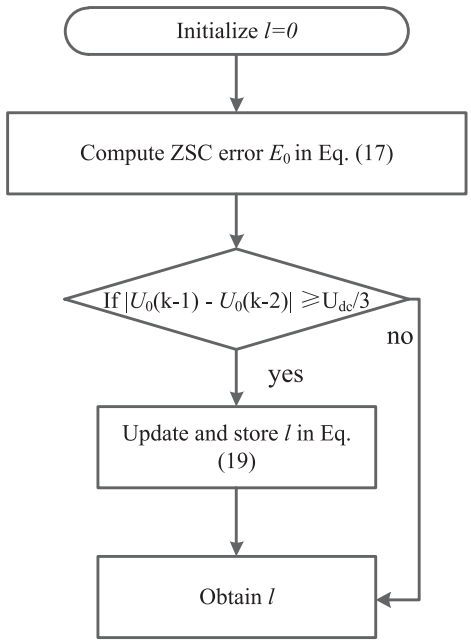

Fig. 6. Flowchart of the acquisition of the parameter *l*.

the predicted ZSC at the $(k+1)$th instant can be obtained as

$$i_0(k+1) = i_0^p(k+1) - \left(E_0(k) + l\left(U_0(k) - U_0(k-1)\right)\right). \tag{22}$$

To consider the one-step delay compensation, the current error $E_0\ (k+2)$ can be obtained as

$$E_0(k+2) \cong \left(\frac{T_s}{\overline{L_0}} - \frac{T_s}{L_0}\right)\left(U_0^{\mathrm{sw}=i}(k+1) - U_0(k)\right) + E_0(k+1). \tag{23}$$

The new predicted ZSC equation at the $(k+2)$th instant can also be obtained as

$$i_0(k+2) = i_0^p(k+2) - E_0(k+2). \tag{24}$$

Substituting (21) and (23) in (24), the predicted ZSC at the $(k+2)$th instant can be obtained as

$$i_0(k+2) = i_0^p(k+2) - \left(E_0(k) + l\left(U_0^{\mathrm{sw}=i}(k+1) - U_0(k-1)\right)\right). \tag{25}$$

After obtaining the predicted ZSC at the $(k+2)$th instant, an optimal switching state can be obtained according to the minimum value of cost function in (15). The diagram of the improved FS-MPCC scheme and the time sequence in the proposed method are shown in Figs. 7 and 8, respectively.

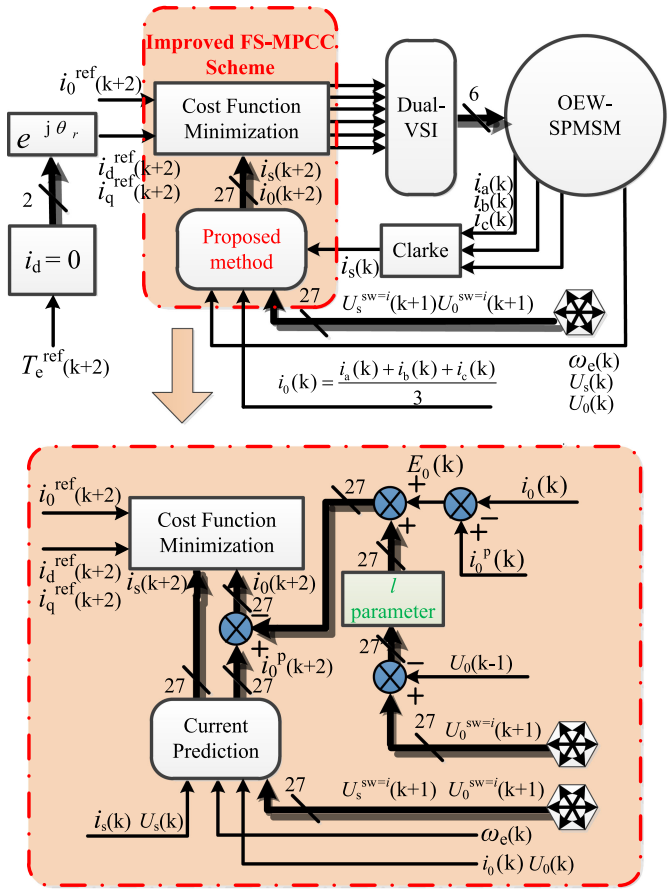

Fig. 7. Improved FS-MPCC scheme with zero-sequence parameter disturbance suppression.

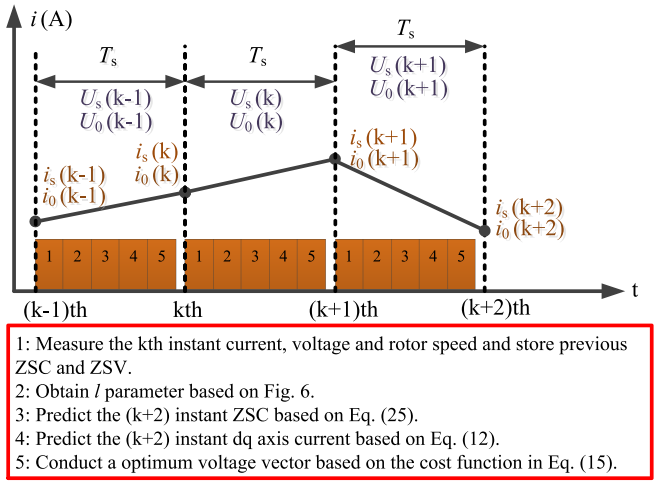

Fig. 8. Diagram of the time sequence for the improved FS-MPCC scheme.

VI. Simulation Study

The proposed FS-MPCC (Method 2) and conventional FS-MPCC (Method 1) are validated in MATLAB/Simulink software. The current sampling time and control period are set to 50 μs. OEW-SPMSM parameters are listed in Table II. Because SPMSM is adopted as a control object, $i_d = 0$ current control is adopted to validate the correctness of the two methods in the simulation and experiment.

First, to testify the aforementioned assumption that the value of the variation of ZSC at the adjacent sampling instant is much smaller than the value of the minimum variation of ZSV at the adjacent sampling instant, $E_0(k) - E_0(k-1)$ (Term

TABLE II
OEW-SPMSM PARAMETERS

Parameter	Description	Value
P_N (kW)	Rated power	1
p	Number of pole pairs	4
R_S (Ω)	Stator resistance	1.38
L_S (mH)	Stator inductance	3.21
Ψ_m (Wb)	Rotor flux linkage	0.1667
T_N (N·m)	Rated torque	4
L_0 (mH)	Zero-sequence inductance	3.1
Ψ_{3m} (Wb)	Zero-sequence rotor flux linkage	0.0074
I_N (A)	Rated Current	4

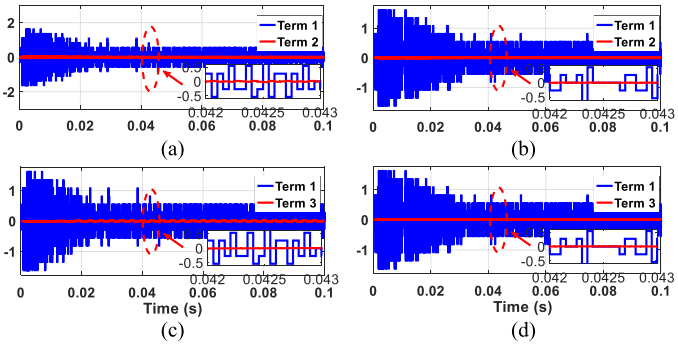

Fig. 9. Simulation results of the comparison from to 1500 r/min. (a) Value of terms 1 and 2. (b) Value of terms 1 and 2. (c) Value of terms 1 and 3. (d) Value of terms 1 and 3.

1), $(\frac{T_s\overline{R_s}}{\overline{L_0}} - \frac{T_sR_s}{L_0})(i_0(k-1) - i_0(k-2))$ (Term 2), and $(\frac{T_s\psi_{3m}}{L_0} - \frac{T_s\overline{\psi_{3m}}}{\overline{L_0}})(3\omega_e(k-1)\sin(3\theta_r(k-1)) - 3\omega_e(k-2)\sin(3\theta_r(k-2)))$ (Term 3) is observed in Fig. 9. Fig. 9(a) denotes the $\overline{R_s} = 10R_s$, $\overline{L_0} = 2\ L_0$ condition from 0 to 1500 r/min in Method 2; Fig. 8(b) denotes the $\overline{R_s} = 0.1R_s$, $\overline{L_0} = 2\ L_0$ condition from 0 to 1500 r/min in Method 2; Fig. 9(c) denotes the $\overline{\Psi_{3m}} = 2\ \Psi_{3m}$, $\overline{L_0} = 2\ L_0$ condition from 0 to 1500 r/min in Method 2; Fig. 9(d) denotes the $\overline{\Psi_{3m}} = 0.5\ \Psi_{3m}$, $\overline{L_0} = 2\ L_0$ condition from 0 to 1500 r/min in Method 2. From the results, it can be found that the value of Term 1 is larger than the value of Terms 2 and 3 under different conditions, while the adjacent ZSVs are different. Therefore, the assumption of (18) can be satisfied in the simulation results.

In addition, the parameter l in Method 2 is observed in Figs. 10 and 11. In the figures, l is computed according to Fig. 6 and the reference l is computed through the term $\frac{T_s}{\overline{L_0}} - \frac{T_s}{L_0}$, which is accurate. From these results, it can be found that the parameter l can track the reference parameter l well under $\overline{L_0} = 2\ L_0, \overline{L_0} = 0.5\ L_0, \overline{L_0} = L_0/3$, and $\overline{L_0} = 3\ L_0$ conditions, which can validate the correctness of the new mechanism.

Finally, to observe the performance at transient and steady state, the results of two methods under $\overline{L_0} = 0.5\ L_0$ condition are presented in Fig. 12. The load torque is 1 N·m at 0.02 s. After that, it is set from 4 to 2 N·m. The normalized mean square errors of d-axis currents for both methods are 0.25 and

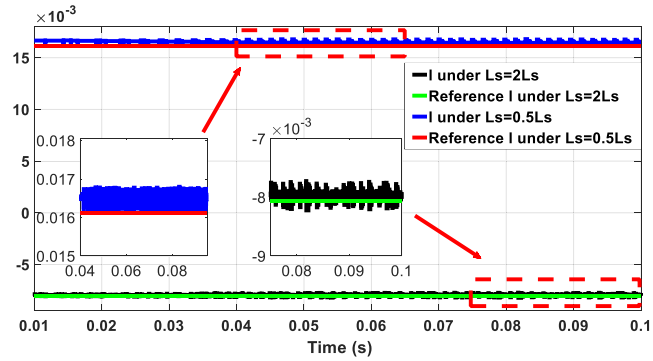

Fig. 10. Simulation results of the comparison of the parameter l and reference parameter l under $\overline{L_0} = 2\ L_0, \overline{L_0} = 0.5\ L_0$ condition.

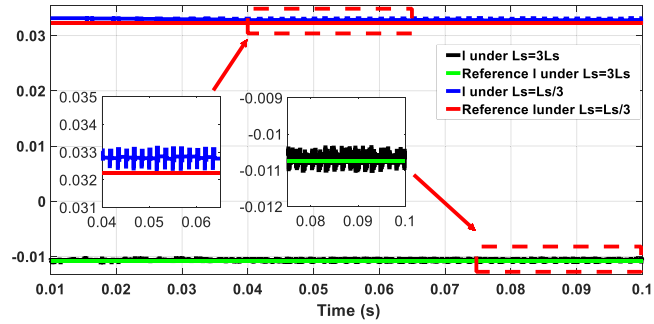

Fig. 11. Simulation results of the comparison of the parameter l and reference parameter l under $\overline{L_0} = L_0/3,\ \overline{L_0} = 3\ L_0$ condition.

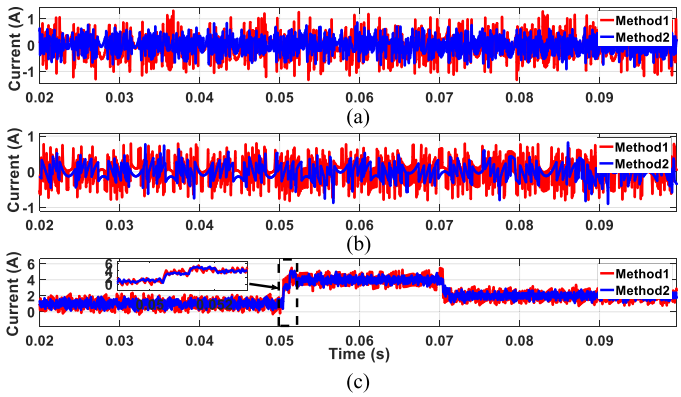

Fig. 12. Simulation results of the comparison at 600 r/min. (a) Current in d-axis. (b) ZSC. (c) Current in q-axis.

0.14, respectively. The normalized mean square errors of q-axis currents for both methods are 0.44 and 0.21, respectively. It can be seen that the zero-sequence model can affect the dq-axis currents performance. Moreover, the normalized mean square errors of ZSC are 0.25 and 0.11, respectively. In addition, the response time (2 ms) is almost the same for the two methods at transient state, and the value of transient oscillation in Method 1 is little bit larger than that in Method 2. Therefore, Method 2 can suppress the disturbance and have better performance with respect to Method 1.

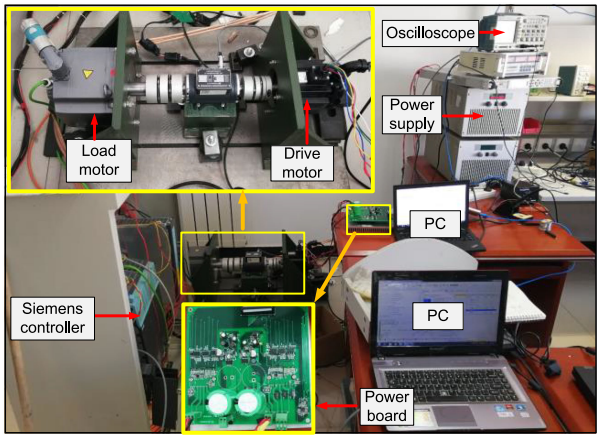

Fig. 13. Diagram of the test rig for OEW-SPMSM drives.

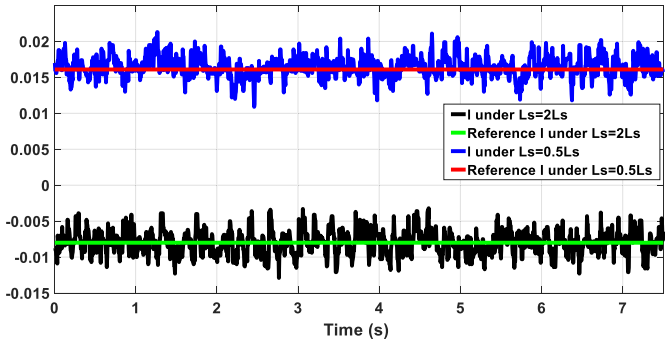

Fig. 14. Experimental results of the comparison of the parameter l and reference parameter l under $\overline{L_0} = 2\ L_0,\ \overline{L_0} = 0.5\ L_0$ condition.

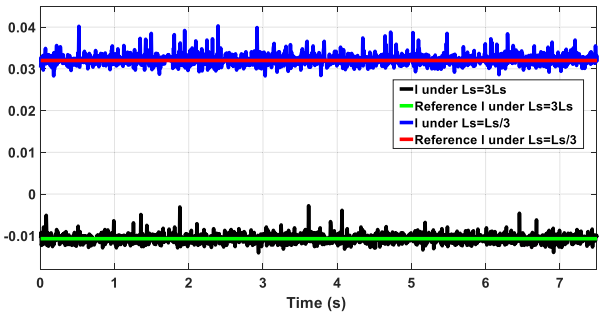

Fig. 15. Experimental results of the comparison of the parameter l and reference parameter l under $\overline{L_0} = L_0/3,\ \overline{L_0} = 3\ L_0$ condition.

VII. Experimental Results

Methods 1 and 2 are also carried out on a dual two-level inverter OEW-SPMSM test rig. Fig. 13 shows the test rig that includes a load motor, OEW-SPMSM, OEW-SPMSM controller, power supply (310 V/10 A), auxiliary power supply (15 V/2 A), oscilloscope, DSP emulator, Siemens controller, which is applied to control the load motor, and two PCs. The controller's main control chip is TMS320F28377d, and a type of FNC42060F is used as a power devices.

Similar to the simulation, the value of parameter l in Method 2 is observed in Figs. 14 and 15 under different conditions. In Fig. 14, the speed is set to 900 r/min and load torque is set to 3 N·m, it can be seen that the parameter l can track the actual value well under $\overline{L_0} = 2\ L_0,\ \overline{L_0} = 0.5\ L_0$ condition. It should be noted that the initial nominal zero-sequence parameters are determined offline. When the test under parameter mismatch needs to be done, zero-sequence parameters can be modified to satisfy the test parameter mismatch condition. When the speed is reduced to 400 r/min, the parameter l also can track the actual value well under $\overline{L_0} = 3\ L_0,\ \overline{L_0} = L_0/3$ condition in Fig. 15. It should be noted that there are some ZSC and ZSV measurement errors in the practical system, which can deteriorate the parameter l performance compared with the simulation results.

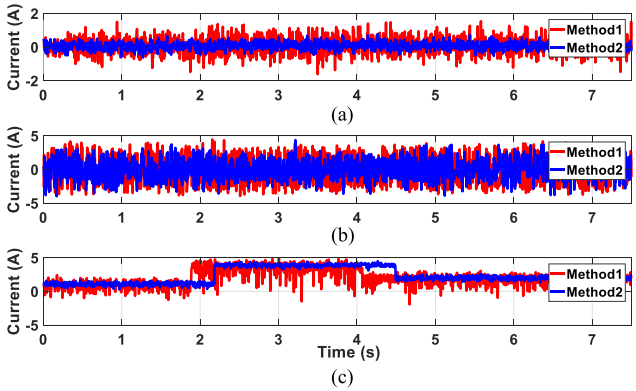

Fig. 16. Experimental results of the comparison at 600 r/min under $\overline{L_0} = 0.5\ L_0$ condition. (a) Current in d-axis. (b) ZSC. (c) Current in q-axis.

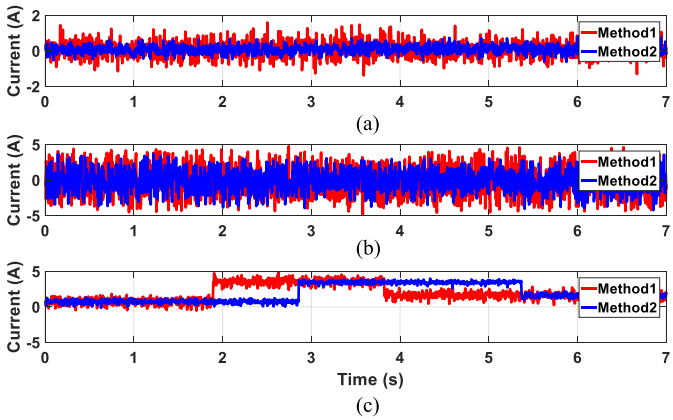

Fig. 17. Experimental results of the comparison at 600 r/min under $\overline{R_0} = 0.1\ R_0$ condition. (a) Current in d-axis. (b) ZSC. (c) Current in q-axis.

To observe the performance at transient and steady state, the results of two methods under different conditions are presented in Figs. 16–18. The load torque begins from 1 to 4 N·m and then it is turned to 2 N·m. In Fig. 16, it can be seen that zero-sequence parameters can actually affect the performance of ZSC and dq-axis currents in Method 1 too much under zero-sequence inductance parameter mismatch condition. The normalized mean square errors of ZSC are 1.44 and 0.78, respectively. In Fig. 17, the normalized mean square errors of ZSC and dq-axis currents in Method 2 are also smaller than that in Method 1 when resistance parameter mismatches. The normalized mean square errors of ZSC are 1.77 and 0.75, respectively. In Fig. 18, a better

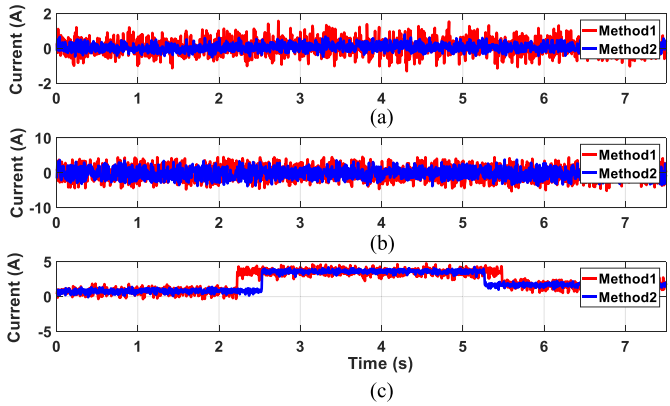

Fig. 18. Experimental results of the comparison from 600 r/min under $\overline{\Psi_{3m}} = 2\Psi_{3m}$. (a) Current in d-axis. (b) ZSC. (c) Current in q-axis.

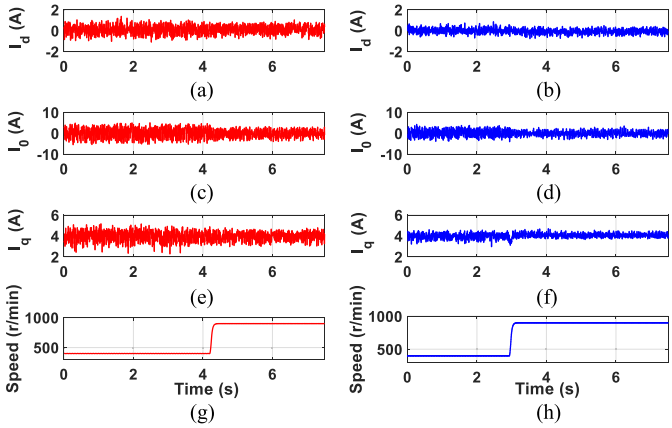

Fig. 19. Experimental results of the comparison from 400 to 900 r/min under $\overline{\Psi_{3m}} = 2\Psi_{3m}, \overline{R_0} = 10\ R_0$, and $\overline{L_0} = 2L_0$ condition. (a) Current in d-axis in Method 1. (b) Current in d-axis in Method 2. (c) ZSC in Method 1. (d) ZSC in Method 2. (e) Current in q-axis in Method 1. (f) Current in q-axis in Method 2. (g) Speed in Method 1. (h) Speed in Method 2.

current performance is in Method 2 when the zero-sequence flux linkage parameter mismatches. The normalized mean square errors of ZSC are 1.59 and 0.81, respectively. Therefore, it can testify that Method 2 can suppress the disturbances caused by zero-sequence parameters. From Fig. 19, the speed is set from 400 to 900 r/min and the current is set to 4 A. Compared with method 2, it can be seen that there are some current peaks in Method 1 under $\overline{R_0} = 10\ R_0$, $\overline{\Psi_{3m}} = 2\ \Psi_{3m}$, and $\overline{L_0} = 2\ L_0$ condition. The parameter mismatch disturbances can be effectively suppressed in Method 2. From Fig. 20, it can be seen that the performance is improved when Method 1 is switched to Method 2 under $\overline{\Psi_{3m}} = 0.5\ \Psi_{3m}$, $\overline{R_0} = 0.1\ R_0$, and $\overline{L_0} = 2\ L_0$ condition. Furthermore, to assess the performance of torque ripple suppression, a mean absolute error M_T as referred to [30], is defined as the assessment criteria:

$$M_T = \frac{1}{N}\sum_{k=1}^{N}|e_T(\mathrm{k})| = \frac{1}{N}\sum_{k=1}^{N}|T_{\mathrm{load}}(\mathrm{k}) - T_e(\mathrm{k})| \qquad (26)$$

where $T_{\mathrm{load}}\ (k)$ and $T_e(k)$ represent the target torque and measured electromagnetic torque, respectively; N denotes the total number of sampling points. From Fig. 21(a), the load torque is

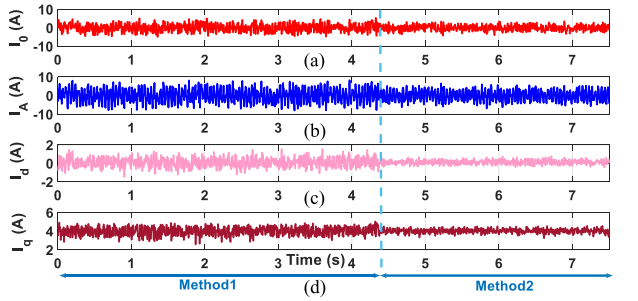

Fig. 20. Experimental results of the comparison from 600 r/min under $\overline{\Psi_{3m}} = 0.5\ \Psi_{3m}$, $\overline{R_0} = 0.1\ R_0$, and $\overline{L_0} = 2\ L_0$ condition. (a) ZSC. (b) Current i_A in A phase stator current. (c) Current in d-axis. (d) Current in q-axis.

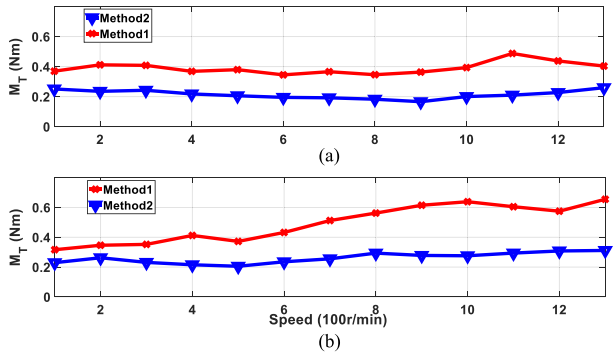

Fig. 21. Experimental results for M_T under different conditions and the load torque is set to 4 N·m. (a) $\overline{\Psi_{3m}} = 2\ \Psi_{3m}$, $\overline{R_0} = 10R_0$, and $\overline{L_0} = 2L_0$ condition. (b) $\overline{\Psi_{3m}} = 0.5\ \Psi_{3m}$, $\overline{R_0} = 0.1\ R_0$, and $\overline{L_0} = 0.5L_0$ condition.

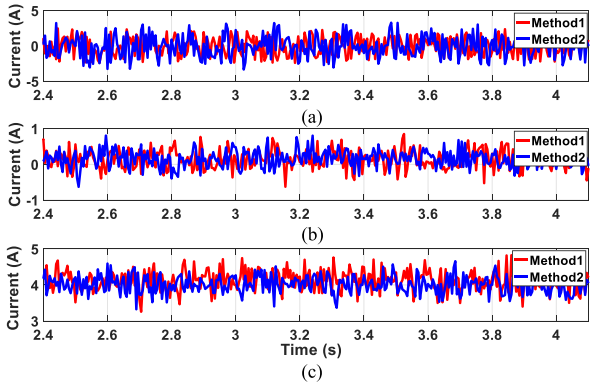

Fig. 22. Experimental results of the comparison at 600 r/min without parameter mismatch. (a) ZSC. (b) Current in d-axis. (c) Current in q-axis.

set to 3 N·m, and the lowest torque ripples occur in Method 2 under different speed conditions. In addition, From Fig. 21(b), it can be seen that the torque ripples are reduced dramatically under $\overline{\Psi_{3m}} = 0.5\ \Psi_{3m}$, $\overline{R_0} = 0.1\ R_0$, and $\overline{L_0} = 0.5\ L_0$ condition in Method 2. Therefore, Method 2 demonstrated the ability to suppress torque ripples caused by zero-sequence parameter disturbances. The steady-state current performance is shown in Fig. 22. It can be seen that the values of dq-axis currents and ZSC are approximately equal in the two methods without parameter mismatch, which can testify that the proposed model can almost have the same current performance with the accurate zero-sequence machine model.

VIII. Conclusion

The academic contributions of this article regarding the suppression of zero-sequence parameter disturbance for OEW-SPMSM are summarized as follows. 1) A novel zero-sequence model is proposed to enhance the proposed FS-MPCC robustness. It can be seen that the novel model parameter can be estimated precisely without using any zero-sequence model parameters in the simulation and experimental results. It is important step toward improved performance drives. 2) An improved FS-MPCC scheme with ZSC suppression is proposed. From the comparative results, the conventional FS-MPCC scheme with ZSC suppression cannot suppress parameter mismatch under different conditions. Moreover, it can be seen that the zero-sequence parameters can deteriorate the torque ripples and the ZSC performance, respectively. On the contrary, the proposed FS-MPCC scheme possesses the capability of zero-sequence parameter disturbances suppression and can be experimentally applied in practical systems, which is a significant step towards FS-MPCC scheme with ZSC suppression for SPMSM drives.

References

[1] M. Mengoni, A. Amerise, and G. Rizzoli, "Control system for open-end winding sync-rel motors with a floating capacitor bridge," in *Proc. Annu. Conf. IEEE Ind. Electron. Soc.*, Oct. 2018, pp. 5695–5701.

[2] B. Reddy and V. T. Somasekhar, "A space-vector modulation scheme for a four-level dual inverter fed open-end winding induction motor drive," in *Proc. IEEE India Int. Conf. Power Electron.*, Dec. 2012, pp. 1–6.

[3] A. Amerise, L. Rovere, and A. Formentini, "Control system for open-end winding surface PM synchronous machines with a floating capacitor bridge," in *Proc. IEEE Energy Convers. Congr. Expo.*, Sep. 2018, pp. 6585–6591.

[4] S. Chowdhury, P. W Wheeler, C. Patel, and C. Gerada, "A multilevel converter with a floating bridge for open-end winding motor drive applications," *IEEE Trans. Ind. Electron.*, vol. 63, no. 9, pp. 5366–5375, Sep. 2016.

[5] C. Min and S. Dan, "A unified space vector pulse width modulation for dual two-level inverter system," *IEEE Trans. Power Electron.*, vol. 32, no. 2, pp. 889–893, Jun. 2016.

[6] Y. He, Y. Zhou, and H. Nian, "Control strategy for open winding PMSM system supplied by the Z-source and voltage source integrated converters," in *Proc. Int. Conf. Elect. Mach. Syst.*, Nov. 2016, pp. 1–6.

[7] B. Li, C. Li, F. Guo, Y. Xin, C. Wang, and X. Pang, "Coordination of Superconductive fault current limiters with zero-sequence current protection of transmission lines," *IEEE Trans. Appl. Supercond.*, vol. 24, no. 5, pp. 889–893, Oct. 2014.

[8] X. Zhang and K. Wang, "Current prediction based zero sequence current suppression strategy for the semi-controlled open-winding PMSM generation system with a common DC Bus," *IEEE Trans. Ind. Electron.*, vol. 65, no. 8, pp. 6066–6076, Aug. 2018.

[9] M. R. Baiju, K. K. Mohapatra, R. S. Kanchan, and K. Gopakumar, "A dual two-level inverter scheme with common mode voltage elimination for an induction motor drive," *IEEE Trans. Power Electron.*, vol. 19, no. 3, pp. 794–805, May 2004.

[10] V. T. Somasekhar and S. Srinivas, "Effect of zero-vector placement in a dual-inverter fed open-end winding induction motor drive with alternate sub-hexagonal center PWM switching scheme," *IEEE Trans. Power Electron.*, vol. 23, no. 3, pp. 1584–1591, May 2008.

[11] V. T. Somasekhar and S. Srinivas, "Effect of zero-vector placement in a dual-inverter fed open-end winding induction-motor drive with a decoupled space-vector PWM strategy," *IEEE Trans. Ind. Electron.*, vol. 55, no. 6, pp. 2497–2505, Jun. 2008.

[12] E. Un and A. M. Hava, "A near-state PWM method with reduced switching losses and reduced common-mode voltage for three-phase voltage source inverters," *IEEE Trans. Ind. Appl.*, vol. 45, no. 2, pp. 782–793, Mar./Apr. 2009.

[13] A. Kiadehi, K. Drissi, and C. Pasquier, "Adapted NSPWM for single DC-link dual-inverter fed open-end motor with negligible low-order harmonics and efficiency enhancement," *IEEE Trans. Power Electron.*, vol. 31, no. 12, pp. 8271–8281, Dec. 2016.

[14] Y. Zhou and H. Nian, "Zero-sequence current suppression strategy of open-winding PMSG system with common DC bus based on zero vector redistribution," *IEEE Trans. Ind. Electron.*, vol. 62, no. 6, pp. 3399–3408, Jun. 2015.

[15] Y. Wang, D. Panda, T. A. Lipo, and D. Pan, "Open-winding power conversion systems fed by half-controlled converters," *IEEE Trans. Power Electron.*, vol. 28, no. 5, pp. 2427–2436, May 2013.

[16] J. C. Hwang and H. T. Wei, "The current harmonics elimination control strategy for six-leg three-phase permanent magnet synchronous motor drives," *IEEE Trans. Power Electron.*, vol. 29, no. 6, pp. 3032–3040, Jun. 2014.

[17] H. Nian and W. Hu, "Torque ripple suppression method with reduced switching frequency for open-winding PMSM drives with common DC BUS," *IEEE Trans. Ind. Electron.*, vol. 66, no. 1, pp. 674–684, Jan. 2019, doi: 10.1109/TIE.2018.2833803.

[18] V. Oleschuk, A. Sizov, B. K. Bose, and A.M. Stankovic, "Phase-shift-based synchronous modulation of dual inverters for an open-end winding motor drive with elimination of zero sequence currents," in *Proc. Int. Conf. Power Electron. Drives Syst.*, Dec. 2005, pp. 325–330.

[19] Q. An, J. Liu, and Z. Peng, "Dual-space vector control of open-end winding permanent magnet synchronous motor drive fed by dual inverter," *IEEE Trans. Power Electron.*, vol. 31, no. 12, pp. 8329–8342, Dec. 2016.

[20] A. V. Sant, K. R. Rajagopal, and N. K. Sheth, "Permanent magnet synchronous motor drive using hybrid pi speed controller with inherent and noninherent switching functions," *IEEE Trans. Magn.*, vol. 47, no. 10, pp. 4088–4091, Oct. 2011.

[21] Y. Zhang and H. Yang, "Model-predictive flux control of induction motor drives with switching instant optimization," *IEEE Trans. Ener. Convers.*, vol. 30, no. 3, pp. 1113–1122, Sep. 2015.

[22] T. G. Habetler, F. Profumo, and M. Pastorelli, "Direct torque control of induction machines using space vector modulation," *IEEE Trans. Power Electron.*, vol. 28, no. 5, pp. 1045–1053, Sep./Oct. 1992.

[23] X. Yuan, S. Zhang, and C. Zhang, "Improved model predictive current control for SPMSM drives with parameter mismatch," *IEEE Trans. Ind. Electron.*, vol. 67, no. 2, pp. 852–862, Feb. 2017.

[24] X. Yuan, C. Zhang, and S. Zhang, "A novel deadbeat predictive current control scheme for OEW-PMSM Drives," *IEEE Trans. Power Electron.*, vol. 34, no. 12, pp. 11990–12000, Dec. 2019, doi: 10.1109/TPEL.2019.2904387.

[25] B. Zhu, K. Rajashekara, and H. Kubo, "A novel predictive current control for open-end winding induction motor drive with reduced computation burden and enhanced zero sequence current suppression," in *Proc. Appl. Power Electron. Conf. Expo.*, May 2017, pp. 552–557.

[26] S. Chong, D. Sun, Z. Zheng, and H. Nian, "Simplified model predictive control for dual-inverter fed open-winding permanent magnet synchronous motor," *IEEE Trans. Energy Convers.*, vol. 33, no. 4, pp. 1846–1854, Dec. 2018, doi: 10.1109/TEC.2018.2841012.

[27] S. Vazquez, J. I. Leon, L. G. Franquelo, and J. Rodriguez, "Model predictive control: a review of its applications in power electronics," *IEEE Ind. Mag.*, vol. 8, no. 1, pp. 16–31, Mar. 2014.

[28] G. Feng, C. Lai, J. Tjong, and N. Kar, "Noninvasive kalman filter based permanent magnet temperature estimation for permanent magnet synchronous machines," *IEEE Trans. Power Electron.*, vol. 33, no. 12, pp. 10673–10682, Dec. 2018.

[29] D. D. Reigosa, D. Fernandez, H. Yoshida, K. Kato, and F. Briz, "Permanent-magnet temperature estimation in PMSMs using pulsating high-frequency current injection," *IEEE Trans. Ind. Appl.*, vol. 51, no. 4, pp. 3159–3168, Jul./Aug. 2015.

[30] X. Zhang, B. Hou, and Y. Mei, "Deadbeat predictive current control of permanent-magnet synchronous motors with stator current and disturbance observer," *IEEE Trans. Power Electron.*, vol. 32, no. 5, pp. 3818–3834, May 2017.

[31] F. Mwasilu, H. Nguyen, H. C. Han, and J. W. Jung, "Finite set model predictive control of interior PM Synchronous motor drives with an external disturbance rejection technique," *IEEE/ASME Trans. Mech.*, vol. 22, no. 2, pp. 762–773, Apr. 2017.

[32] X. Yuan, S. Zhang, and C. Zhang, "Torque ripple suppression for open-end winding permanent-magnet synchronous machine drives with predictive current control," *IEEE Trans. Ind. Electron.*, to be published, doi: 10.1109/TIE.2019.2907506.

Xin Yuan was born in Heilongjiang, China, in 1990. He received the B.Eng. and M.Sc. degrees in electrical engineering, in 2013 and 2016, respectively. He is currently working toward the Ph.D. degree with the National Engineering Laboratory for Electric Vehicles and School of Mechanical Engineering, Beijing Institute of Technology, Beijing, China.

He has been a Research Associate with Power Electronics, Machines and Control Group, University of Nottingham, Nottingham, U.K., since January 2019. His research interests include synchronous motor drives, power converters, multiphase motor drives, and fault-tolerant strategy of motor.

Shuo Zhang received the B.Eng. degree from the North China Institute of Aerospace Engineering, Hebei, China, in 2011, and the Ph.D. degree in vehicle engineering from the Beijing Institute of Technology, Beijing, China, in 2017.

He is currently an Assistant Professor with the National Engineering Laboratory for Electric Vehicles and School of Mechanical Engineering, Beijing Institute of Technology. His research interests include the modeling and control for the permanent magnet synchronous motor, multimotor driving system, and hybrid power system.

Chengning Zhang received the M.E. degree in control theory and control engineering and the Ph.D. degree in vehicle engineering from the Beijing Institute of Technology, Beijing, China, in 1989 and 2001, respectively.

He is currently a Professor and the Vice Director of the National Engineering Laboratory for Electric Vehicles, Beijing Institute of Technology. His research interests include electric vehicles, vehicular electric motor drive systems, battery management systems, and chargers.

Michele Degano (M'15) received the Laurea degree in electrical engineering from the University of Trieste, Trieste, Italy, in 2011, and the Ph.D. degree in industrial engineering from the University of Padova, Padova, Italy, in 2015.

In 2015, he was a Research Fellow with the Power Electronics, Machines and Control Group, The University of Nottingham, Nottingham, U.K., where he is currently an Assistant Professor teaching advanced courses on electrical machines. His main research interests include design and optimization of permanent-magnet machines, reluctance and permanent-magnet-assisted synchronous reluctance motors through genetic optimization techniques, for automotive and aerospace applications.

Giampaolo Buticchi (S'10–M'13–SM'17) received the master's degree in electronic engineering and the Ph.D degree in information technologies from the University of Parma, Parma, Italy, in 2009 and 2013, respectively.

In 2012, he was a Visiting Researcher with The University of Nottingham, Nottingham, U.K. Between 2014 and 2017, he was a Postdoctoral Researcher and Von Humboldt Postdoctoral Fellow with the University of Kiel, Kiel, Germany.

He is currently an Associate Professor in electrical engineering with The University of Nottingham Ningbo China, Ningbo, China, and the Head of Power Electronics of the Nottingham Electrification Center, Nottingham, U.K. He is the author/co-author of more than 190 scientific papers. His research focuses on power electronics for renewable energy systems, smart transformer fed microgrids, and dc grids for the More Electric Aircraft..

Dr. Buticchi is currently an Associate Editor for the IEEE TRANSACTIONS ON INDUSTRIAL ELECTRONICS, IEEE Open Journal of the Industrial Electronics Society, and IEEE TRANSACTIONS ON TRANSPORTATION ELECTRIFICATION. He is the Chair of the IEEE Industrial Electronics Society Technical Committee on Renewable Energy Systems.

Alessandro Galassini (S'13–M'17) received the master's degree in mechatronic engineering from the University of Modena and Reggio Emilia, Reggio Emilia, Italy, in 2012, and the Ph.D. degree in power sharing for multi-three-phase electrical machines from the University of Nottingham, Nottingham, U.K., in 2017.

He is currently a Researcher with the Power Electronics, Machines and Control Group, The University of Nottingham. His research interests include control of electrical drives for future transportation systems.